## Role of Scalp EEG Brain Connectivity in Motor Imagery Decoding for BCI Applications \*

Fatemeh Delavari

Biomedical Engineering Department

University of Connecticut

Storrs, CT (USA)

fatemeh.delavari@uconn.edu

Sabato Santaniello
Biomedical Engineering Department
University of Connecticut
Storrs, CT (USA)
sabato.santaniello@uconn.edu

#### Abstract

Brain Connectivity (BC) features of multichannel EEG have been proposed for Motor Imagery (MI) decoding in Brain-Computer Interface applications, but the advantages of BC features vs. single-channel features are unclear. Here, we consider three BC features, i.e., Phase Locking Value (PLV), Granger Causality, and weighted Phase Lag Index, and investigate the relationship between the most central nodes in BC-based networks and the most influential EEG channels in single-channel classification based on common spatial pattern filtering. Then, we compare the accuracy of MI decoders that use BC features in source vs. sensor space. Applied to the BCI Competition VI Dataset 2a (left- vs. right-hand MI decoding), our study found that PLV in sensor space achieves the highest classification accuracy among BC features and has similar performance compared to single-channel features, while the transition from sensor to source space reduces the average accuracy of BC features. Across all BC measures, the network topology is similar in left- vs. right-hand MI tasks, and the most central nodes in BC-based networks partially overlap with the most influential channels in single-channel classification.

**Keywords:** Phase Locking Value, Granger Causality, Phase Lag Index, Graph Analysis, Motor Imagery, Brain-Computer Interface, EEG

<sup>\*</sup>This work was supported in part by the U.S. National Science Foundation under Grant CAREER 1845348. This manuscript is a preprint version of an article published in the proceedings of the 46th Conference of the IEEE Engineering in Medicine and Biology Society (EMBC 2024), DOI: 10.1109/EMBC53108.2024.10781532.

### 1 Introduction

Decoding motor imagery (MI) by using multichannel electroencephalographic (EEG) signals at the scalp is a challenging task in many Brain-Computer Interface (BCI) applications [1]. Several approaches have leveraged event-related desynchronization of EEG rhythms in the mu (8–13 Hz) and beta (18–26 Hz) frequency band that occurs in selected regions of the brain when large body parts are imagined to move [2] but results have often suffered from intra-subject EEG variability [3].

Studies [4–7] have recently proposed to use measures of pairwise functional connectivity between EEG channels as potential features for MI classification, and studies [8–10] have shown that combining brain connectivity (BC) features, deep learning algorithms, and Riemannian geometry can lead to high accuracy both in two- and four-class MI classification. It remains unclear, though, whether BC features have superior predictive power compared to features calculated for single EEG channels. Also, while several classes of BC features have been proposed [3], it is unclear whether brain networks characterized by directed graphs lead to better classification performance compared to networks with undirected graphs, and whether MI decoding based on BC features improves when the brain connectivity is estimated in the source space, i.e., when BC features are computed between putative dipole sources after performing EEG source imaging (ESI), compared to the sensor space.

In this study, we addressed this gap in knowledge by systematically comparing the predictive power of three different sets of BC features in classifying upper-limb MI tasks, where BC features were chosen to measure brain connectivity with both directed and undirected graphs. Moreover, the proposed BC features were computed in sensor space and source space to assess the impact of ESI on BC-based MI classification, and a comparison against classifiers that use single-channel features was conducted to assess the competitive edge of BC features over single-channel features in MI task classification.

#### 2 Materials and Methods

We used multichannel scalp EEG from the BCI Competition IV, dataset 2a [11]. Briefly, 9 healthy individuals performed a motor imagery task during which they were alternatively asked to imagine moving the left hand (LH), right hand (RH), both feet, or their tongue. Every participant completed two sessions on separate days, and 22 electrodes were used for EEG collection in both sessions (monopolar recording; sampling rate: 250 Hz; reference and ground: left and right mastoid, respectively). Each session consisted of 6 repetitions, with a repetition including 12 trials per MI task type, for a total of 72 trials per session for each MI task type (LH, RH, feet, and tongue). Each trial lasted 7.5 s, during which the participants received no feedback, and consisted of a 2-s-long fixation (i.e., a fixation cross appeared on the screen), followed by a go-cue indicating the type of MI task (random assignment). Participants engaged in the MI task at the

appearance of the cue and till the disappearance of the fixation cross, which occurred 4 s after the cue's first appearance. A 1.5-s-long rest period completed the trial.

Here, we only used LH and RH tasks from the first session (144 trials per participant altogether) to enable the comparison against classifiers that use single-channel features based on common spatial pattern (CSP) filtering, whereas CSP filters are mainly defined for two-class scenarios. All analyses were conducted in MATLAB rel. 2021b, The MathWorks, Natick, MA.

#### 2.1 EEG processing and Source Estimation

EEG processing was performed in EEGLAB [12]. Signals were band-pass filtered in the mu (8–13 Hz) frequency band with a zero-phase digital FIR filter, and a notch filter was applied to remove the 60-Hz power line noise. Independent component analysis (ICLabel plugin [13]) was then used to identify and remove muscle, eye, and heart rate artifacts. ICLabel-generated labels were treated as initial guide, and the decision to remove an independent component was made after inspecting the scalp topography, ERP, and power spectrum. EEG signals were then re-referenced (average reference).

To investigate EEG connectivity in source space, we set a reference atlas (ICBM 152) [14], and dipole currents (sources) were calculated on this atlas for every EEG time series. We used Brainstorm [15] for atlas segmentation and mesh grid calculation (1,082, 1,922, and 1,922 vertices for scalp, skull, and brain, respectively), and the cortical surface was parceled into 210 regions as in [16]. For every multichannel EEG time series, dipole currents were calculated in OpenMEEG [17].

#### 2.2 Brain Connectivity Features

For each trial, we focused on the last 3 s of motor imagery, i.e., from 1 s after the go-cue appearance till the disappearance of the fixation cross. For any trial k and pair (r, s) of EEG channels, the following BC measures were computed:

- Phase Locking Value  $PLV_{r,s}(k) = |E(e^{j\Delta\varphi_{rs,k}})|$  [18], where  $E(\cdot)$  is the expected value, and  $\Delta\varphi_{rs,k}$  is the series of phase differences between signals r and s in trial k.
- Granger Causality of r to s,  $GC_{r,s}(k) = \log \sigma_{s,k}^2/\sigma_{rs,k}^2$ , where  $\sigma_{s,k}^2$  is the variance of the error of an autoregressive (AR) model fitting the EEG at channel s in trial k, and  $\sigma_{rs,k}^2$  is the variance of the error of an AR model that fits the EEG at channel s by using prior values at both r and s as input [19].
- Weighted Phase Lag Index [20], which is defined as  $wPLI_{r,s}(k) = |E(\Delta\varphi_{rs,k})|/E(|\Delta\varphi_{rs,k}|)$  and was proposed to reduce the sensitivity to uncorrelated noise sources and detect changes in phase-synchronization between channels.

For every measure W (W = PLV, GC, wPLI), we used the adjacency matrix  $A_k(W) = \{W_{r,s}(k)\}_{r,s}$  as a feature set to predict whether trial k involves RH-MI or LH-MI.

#### 2.3 Single Channel Features and Binary Classifier

For each measure W (W = PLV, GC, wPLI), we used adjacency matrices  $A_k(W)$  as input to a Random Forests (RF) classifier with N decision trees and varied N from 10 to 200 with increments of 10. For any N, five-fold cross-validation was adopted to assess the classification accuracy of RH-MI vs. LH-MI tasks.

To assess whether BC features enhance MI classification accuracy compared to single-channel features, we also trained a RF classifier with N trees receiving a set of 22 features per trial (one per EEG channel), where the feature value,  $f_r(k)$ , of any channel r in trial k is  $f_r(k) = \log \left(\sigma_{x_{r,k}}^2 / \sum_s \sigma_{x_{s,k}}^2\right)$  [21],  $x_{r,k}$  is the EEG time series at channel r in trial k, and  $\sigma_{x_{r,k}}^2$  is the variance of  $x_{r,k}$ . Features  $f_r(k)$  were computed under two conditions, i.e., we first considered the case where  $x_{r,k}$  is the EEG signal obtained after the filtering stage  $(f_r = f_{r,eeg})$ ; then, for each fold of the cross-validation procedure, we used the signals in the training set to estimate the common spatial patterns of the multichannel EEG [22], and  $x_{r,k}$  were obtained by mapping the EEG time series onto the CSP directions  $(f_r = f_{r,csp})$ . For each fold of the cross-validation procedure, CSP filters estimated on training data were also applied to test data.

#### 2.4 Measures of Network Topology

For every measure W (W = PLV, GC, wPLI), we analyzed the brain network topology during RH-MI vs. LH-MI. We calculated the sample distribution of values  $W_{r,s}(k)$  across all combinations of trials and pairs of EEG channels, the corresponding mean  $(\mu_W)$ , and standard deviation  $(\sigma_W)$ . Then, we built the matrix  $\hat{A}_k(W)$  from  $A_k(W)$  by replacing entries  $W_{r,s}(k) > \mu_W + 0.5\sigma_W$  with 1s and the remaining entries with 0s. Finally, the following measures were calculated for  $\hat{A}_k(W)$  and averaged across RH-MI or LH-MI trials, respectively:

- Graph Density GD = 2m/n(n-1), where n is the count of nodes in the network (i.e., EEG channels) and m is the count of edges, i.e., an edge is present between any nodes r and s if the (r, s)-th entry in  $\hat{A}_k(W)$  is 1.
- Shortest Path Length  $SPL = \sum_{r,s} d_{rs}/(n(n-1))$ , where  $d_{rs}$  is the shortest path distance between nodes r and s. SPL measures the integrity of the BC graph [23].
- Clustering Coefficient  $CC = \sum_r 2T_r/(z_r n(z_r 1))$ , where  $T_r$  is the count of neighbor pairs connected to node r, and  $z_r$  is the total number of neighbors of r. CC measures the degree to which nodes tend to cluster together [23].

• PageRank Centrality [23], which measures the importance of each node in the network.

#### 3 Results

Across all subjects and features, the average classification accuracy of the RF classifiers on test data did not significantly improve as the number of decision trees, N, increased above 100. Hence, we set N = 100 in the rest of the study.

# 3.1 PLV Features Provide Superior Classification Accuracy

Table 1 reports the average classification accuracy on test trials for RF classifiers trained on PLV, GC, or wPLI, respectively, for each subject and averaged across all subjects. We found that the accuracy of classifiers that use PLV was significantly higher compared to GC and wPLI (ANOVA one-way test with Tukey's HSD post-hoc test; P-value P < 0.05 and P < 0.01 for PLV vs. GC and PLV vs. WPLI, respectively), while GC and WPLI performed similarly (P > 0.05). Also, PLV-based classifiers had similar performance compared to classifiers using  $f_{r,eeg}$  features, both within subjects and across subjects. Finally, concatenating PLV features and  $f_{r,eeg}$  features (i.e.,  $PLV + f_{r,eeg}$  in Table 1) did not cause a significant enhancement of the classification performance. The application of a CSP filter, instead, resulted in significantly higher accuracy for single-channel features  $f_{r,csp}$  compared to PLV in every subject despite the presence of high variability across folds (P < 0.05).

#### 3.2 MI Tasks Affect the Strength of Network Edges

Figure 1A displays the average Gini importance of features  $f_{r,eeg}$  across all subjects and folds, along with the average change in normalized PageRank centrality for channel r within PLV-based network graphs, comparing right-hand motor imagery (RH-MI) to left-hand motor imagery (LH-MI). Notably, channel Cp4, which is situated above the sensorimotor cortex, exhibits both the highest relevance based on single-channel features and the greatest centrality. Figure 1B-i illustrates the channels with higher Gini importance, and Figure 1B-ii depicts those channels whose network centrality exhibits significant variations between tasks, indicating a substantial overlap. Fig. 1C, instead, shows the mean relative power in the mu frequency band for the EEG channel with the highest Gini importance across all subjects (i.e., Cp4) for trials involving RH-MI and LH-MI. We found that the classification based on single-channel features primarily leverages a decrease in mu power during LH-MI vs. RH-MI. Vice versa, the PLV-based brain network topology did not change significantly across MI tasks, and the global metrics GD, SPL, and CC did not significantly change in RH-MI vs. LH-MI (Table 2, RANOVA test with Greenhouse-Geisser correction) both across subjects (RH-MI vs. LH-MI: P-value P=0.23, P=0.17, and

Table 1: Classification Accuracy of Brain Connectivity Features Versus Single Channel Features

Subject	Accuracy on Test Data (%) <sup>a</sup>					
ID	PLV	GC	wPLI	$f_{r,\text{eeg}}$	PLV	$f_{r, csp}$
					$+f_{r,\text{eeg}}$	
S1	70.17	63.94	61.06	73.55	73.62	73.57
	(10.97)	(9.11)	(9.54)	(7.90)	(8.61)	(9.64)
S2	48.60	40.25	43.15	45.91	50.69	52.67
	(10.24)	(7.74)	(12.14)	(11.21)	(11.54)	(8.96)
S3	86.11	68.74	57.49	88.18	86.77	93.81
	(5.98)	(8.81)	(13.42)	(3.17)	(4.64)	(4.30)
S4	72.88	62.56	54.06	72.27	70.12	78.48
	(4.77)	(14.14)	(10.01)	(6.26)	(7.22)	(4.35)
S5	54.19	53.60	41.67	54.16	57.59	58.48
	(7.30)	(11.20)	(7.34)	(11.54)	(5.11)	(8.99)
S6	61.82	55.64	52.00	55.54	56.85	64.62
	(12.36)	(13.18)	(8.27)	(3.06)	(8.72)	(10.84)
S7	54.80	48.65	54.21	59.70	47.98	73.67
	(9.18)	(6.29)	(5.77)	(8.03)	(8.01)	(4.88)
S8	87.54	73.62	50.00	91.72	84.68	96.52
	(7.51)	(8.61)	(11.04)	(6.26)	(5.43)	(2.36)
S9	57.78	54.88	65.99	63.84	67.24	76.24
	(12.51)	(12.10)	(8.15)	(8.22)	(11.95)	(5.30)
Avg.b	65.99	57.99	53.29	67.21	66.17	74.22
	(15.84)	(13.64)	(11.58)	(16.43)	(15.32)	(15.38)

<sup>&</sup>lt;sup>a</sup>Values are reported as mean (std.dev.). <sup>b</sup> Average across subjects.

P=0.11 for GD, SPL, and CC, respectively) and in each subject (RH-MI vs. LH-MI: P>0.44, P>0.44, and P>0.46 for GD, SPL, and CC respectively).

Altogether, these results indicate that the topographic organization of the brain network, especially when estimated by using measurements of phase synchrony, remains unaltered as the objective of the MI task changes, while a variation to the MI goal affects the average strength of the edges between nodes and results in selective modulation of the node centrality.

#### 3.3 BC Features in Sensor Space Improve Classification

Prior studies in MI-BCI [24] have proposed that EEG source imaging may substantially enhance the performance of a MI decoder. To test whether this would extend to the case of MI classification based on BC features, we performed ESI in each subject. Then, for every trial k, we calculated the average PLV between the dipoles in any pair of cortical regions defined by the parcellation [16] (210 regions altogether) and built the corresponding adjacency matrix (size:

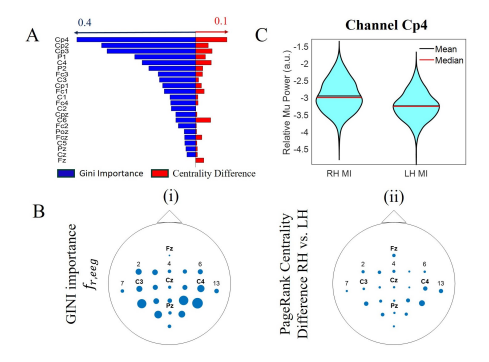


Figure 1: A) Average Gini importance of the EEG channels in LH- vs. RH-MI classification based on single-channel features  $f_{r,\rm eeg}$  (blue bars) and average difference between PageRank centrality values in LH- vs. RH-MI (red bars). Blue and red scale apply to Gini importance and PageRank centrality difference, respectively. B) Average Gini importance (i) and PageRank centrality difference in RH- vs. LH-MI (ii) for EEG nodes are reported in a topographic map. The size of each node is proportional to the node's Gini importance (i) and PageRank centrality difference (ii), respectively. Average values in A-B) are computed across all subjects and folds. C) Relative power in mu band (8–13 Hz) for channel Cp4 in RH- and LH-MI. Violin plots are reported across all subjects and folds.

 $210\times210$ ). Finally, we flattened these matrices and used the resulting vectors as input to a RF classifier with N=100 trees and tested the performance of the RF classifier through a five-fold cross-validation procedure in every subject. Table 3 shows that the classification performance significantly decreased when using PLV features in the source space compared to PLV features calculated in the sensor space (two-sample t-test, P-value P<0.01) both in each subject and across subjects.

Altogether, this indicates that when the number of EEG channels is limited, the combination of ESI and BC features does not necessarily improve the classification of MI tasks, and better results can be achieved in the sensor space.

#### Conclusions

We assessed the effectiveness of various connectivity measures for MI-BCI applications and showed that PLV allows high accuracy in classifying hand motor imagery, especially when classification is done in the EEG sensor space. Our results indicate that motor imagery tasks do not alter the overall topology of the network; instead, they primarily influence the strength of the network's edges.

Table 2: Topology Measures for PLV-based Networks in Left-Hand (LH) Versus Right-Hand (RH) Motor Imagery

Subject	$GD^{\mathrm{a}}$		$SPL^{\mathrm{a}}$		$CC^{\mathrm{a}}$	
ID	LH	RH	LH	RH	LH	RH
S1	0.145	0.158	1.835	1.775	0.089	0.098
	(0.029)	(0.032)	(0.044)	(0.045)	(0.044)	(0.045)
S2	0.151	0.145	1.799	1.840	0.100	0.091
	(0.024)	(0.025)	(0.035)	(0.035)	(0.035)	(0.035)
S3	0.164	0.157	1.749	1.789	0.102	0.087
	(0.034)	(0.034)	(0.043)	(0.047)	(0.043)	(0.047)
S4	0.159	0.157	1.773	1.776	0.105	0.104
	(0.034)	(0.028)	(0.041)	(0.045)	(0.041)	(0.045)
S5	0.148	0.146	1.841	1.842	0.089	0.085
	(0.036)	(0.034)	(0.043)	(0.037)	(0.043)	(0.037)
S6	0.150	0.153	1.815	1.809	0.058	0.061
	(0.034)	(0.034)	(0.037)	(0.038)	(0.037)	(0.038)
S7	0.150	0.150	1.802	1.801	0.083	0.084
	(0.028)	(0.022)	(0.037)	(0.028)	(0.037)	(0.028)
S8	0.159	0.164	1.753	1.746	0.092	0.099
	(0.027)	(0.032)	(0.039)	(0.040)	(0.039)	(0.040)
S9	0.160	0.157	1.771	1.780	0.083	0.089
	(0.037)	(0.032)	(0.044)	(0.039)	(0.044)	(0.039)
Avg.b	0.154	0.154	1.793	1.795	0.088	0.088
	(0.032)	(0.031)	(0.042)	(0.041)	(0.042)	(0.041)

<sup>&</sup>lt;sup>a</sup>Values are reported as mean (std.dev.). <sup>b</sup> Average across subjects.

#### References

- [1] R. Abiri, S. Borhani, E. W. Sellers, Y. Jiang, and X. Zhao, "A comprehensive review of EEG-based brain-computer interface paradigms," J. Neural Eng., vol. 16, no. 1, article 011001, February 2019.
- [2] G. Pfurtscheller and F. H. Lopes da Silva, "Event-related EEG/MEG synchronization and desynchronization: basic principles," Clin. Neurophysiol., vol. 110, no. 11, pp. 1842–1857, November 1999.
- [3] L. Brusini, F. Stival, F. Setti, E. Menegatti, G. Menegaz, and S. F. Storti, "A systematic review on Motor-Imagery brain-connectivity-based computer interfaces," IEEE Trans. Hum. Mach. Syst., vol. 51, no. 6, pp. 725–733, December 2021.
- [4] B. O. Olcay and B. Karacali, "Evaluation of synchronization measures for capturing the lagged synchronization between EEG channels: a cognitive

Table 3: Classification Accuracy of PLV Features in Sensor Space Versus Source Space

Subject	Accuracy on Test Data (%) <sup>a</sup>				
ID	Sensor Space	Source Space			
S1	70.17 (10.97)	60.47 (4.80)			
S2	48.60 (10.24)	45.94 (11.66)			
S3	86.11 (5.98)	75.00 (2.86)			
S4	72.88 (4.77)	37.46 (8.40)			
S5	54.19 (7.30)	44.41 (9.37)			
S6	61.82 (12.36)	68.79 (8.63)			
S7	54.80 (9.18)	41.60 (9.47)			
S8	87.54 (7.51)	56.92 (4.86)			
S9	57.78 (12.51)	52.88 (9.49)			
Avg.b	65.99 (15.84)	53.72 (14.21)			

<sup>&</sup>lt;sup>a</sup>Values are reported as mean (std.dev.). <sup>b</sup> Average across subjects.

task recognition approach," Comput. Biol. Med., vol. 114, article 103441, November 2019.

- [5] K. Georgiadis, N. Laskaris, S. Nikolopoulos, and I. Kompatsiaris, "Connectivity steered graph Fourier transform for motor imagery BCI decoding," J. Neural Eng., vol. 16, no. 5, article 056021, August 2019.
- [6] D. Rathee, H. Cecotti, and G. Prasad, "Single-trial effective brain connectivity patterns enhance discriminability of mental imagery tasks," J. Neural Eng., vol. 14, no. 5, article 056005, October 2017.
- [7] L. F. S. Uribe et al., "A correntropy-based classifier for motor imagery brain-computer interfaces," Biomed. Phys. Eng. Express, vol. 5, no. 6, article 065026, November 2019.
- [8] K. Samanta, S. Chatterjee, and R. Bose, "Cross-subject motor imagery tasks EEG signal classification employing multiplex weighted visibility graph and deep feature extraction," IEEE Sens. Lett., vol. 4, no. 1, pp. 1–4, January 2020.
- [9] F. Shamsi, A. Haddad, and L. Najafizadeh, "Early classification of motor tasks using dynamic functional connectivity graphs from EEG," J. Neural Eng., vol. 18, no. 1, article 016015, February 2021.
- [10] F. S. Racz et al., "Combining detrended cross-correlation analysis with Riemannian geometry-based classification for improved brain-computer interface performance," Front. Neurosci.", vol. 18, article 1271831, March 2024.

- [11] M. Tangermann *et al.*, "Review of the BCI Competition IV," Front. Neurosci.", vol. 6, article 55, July 2012.
- [12] A. Delorme and S. Makeig, "EEGLAB: an open source toolbox for analysis of single-trial EEG dynamics including independent component analysis," J. Neurosci. Methods, vol. 134, no. 1, pp. 9–21, March 2004.
- [13] L. Pion-Tonachini, K. Kreutz-Delgado, and S. Makeig, "ICLabel: an automated electroencephalographic independent component classifier, dataset, and website," Neuroimage, vol. 198, pp. 181–197, September 2019.
- [14] V. Fonov *et al.*, "Unbiased average age-appropriate atlases for pediatric studies," Neuroimage, vol. 54, no. 1, pp. 313–327, January 2011.
- [15] F. Tadel, S. Baillet, J. C. Mosher, D. Pantazis, and R. M. Leahy, "Brainstorm: a user-friendly application for MEG/EEG analysis," Comput. Intell. Neurosci., vol. 2011, article 879716, April 2011.
- [16] L. Fan et al., "The human Brainnetome atlas: a new brain atlas based on connectional architecture," Cereb. Cortex, vol. 26, no. 8, pp. 3508–3526, August 2016.
- [17] A. Gramfort, T. Papadopoulo, E. Olivi, and M. Clerc, "OpenMEEG: open-source software for quasistatic bioelectromagnetics," Biomed. Eng. Online, vol. 9, no. 1, article 45, September 2010.
- [18] J. P. Lachaux, E. Rodriguez, J. Martinerie, and F. J. Varela, "Measuring phase synchrony in brain signals," Hum. Brain Mapp., vol. 8, no. 4, pp. 194–208, November 1999.
- [19] A. Muller, J. F. Kraemer, T. Penzel, H. Bonnemeier, J. Kurths, and N. Wessel, "Causality in physiological signals," Physiol. Meas., vol. 37, no. 5, pp. R46–R72, May 2016.
- [20] M. Vinck, R. Oostenveld, M. van Wingerden, F. Battaglia, and C. M. Pennartz, "An improved index of phase-synchronization for electrophysiological data in the presence of volume-conduction, noise and sample-size bias," Neuroimage, vol. 55, no. 4, pp. 1548–1565, April 2011.
- [21] H. Ramoser, J. Muller-Gerking, and G. Pfurtscheller, "Optimal spatial filtering of single trial EEG during imagined hand movement," IEEE Trans. Rehabil. Eng., vol. 8, no. 4, pp. 441–446, December 2000.
- [22] Z. J. Koles, "The quantitative extraction and topographic mapping of the abnormal components in the clinical EEG," Electroencephalogr. Clin. Neurophysiol., vol. 79, no. 6, pp. 440–447, December 1991.
- [23] M. E. J. Newman, Networks: An Introduction. New York, NY: Oxford University Press, 2010.

[24] B. J. Edelman, B. Baxter, and B. He, "EEG source imaging enhances the decoding of complex right-hand motor imagery tasks," IEEE Trans. Biomed. Eng., vol. 63, no. 1, pp. 4–14, January 2016.